Journal of Applied Polymer Science

Elastic constants of lamellar and interlamellar regions in α and mesomorphic isotactic polypropylene by AFM indentation

R. C. Picu, A. R. Osta
Department of Mechanical, Aerospace, and Nuclear Engineering, Rensselaer Polytechnic Institute, Troy, New York 12180
Correspondence to: A. Osta (E-mail: osta@rowan.edu)

ABSTRACT: A study of the nanoscale mechanical properties of isotactic mesomorphic and semi-crystalline polypropylene (iPP) is presented. Two iPPs produced with metallocene and Ziegler-Natta catalyst polymerization are used. The resulting fibers are characterized by wide angle X-ray scattering, small-angle X-ray scattering (SAXS), and Raman spectroscopy. The spatial variability of the percentage crystallinity is evaluated based on the SAXS data. AFM indentation is performed to measure the elastic modulus of the fibers in the direction perpendicular and parallel to the fiber axis. Since the AFM probing is performed on a scale larger than the lamellar thickness, a statistical analysis of the AFM and SAXS data is necessary to infer the elastic moduli of the α crystals and of the inter-lamellar regions. The elastic modulus of the crystalline lamellae in the direction perpendicular to the c-axis of the α crystal probed in compression is estimated at approximately 3.3 GPa, while the effective modulus of the interlamellar regions ranges from 1.5 to 2.2 GPa. The method proposed can be applied to other material systems with similar layered structure to measure elastic moduli or hardness on length scales smaller than the resolution of the indentation test. © 2016 Wiley Periodicals, Inc. J. Appl. Polym. Sci. **2016**, *133*, 43649.

KEYWORDS: fibers; morphology; polyolefins; structure-property relations; theory and modeling

Received 7 January 2016; accepted 15 March 2016
DOI: 10.1002/app.43649

INTRODUCTION

Isotactic polypropylene exists in the amorphous, crystalline and the defective/mesomorphic phase. Quiescent crystallization from the melt or solidification under flow at low flow rates leads to a spherulitic semicrystalline structure. As the deformation rate increases, the spherulitic structure transitions to the shish–kebab structure, which is composed from a set of strongly aligned chains, the "shish," and lamellae similar to those forming the spherulites, which nucleate on the shish and grow perpendicular to it, the "kebab."

The crystal phase has three predominant polymorphs which form in specific conditions of pressure and temperature.[1] The monoclinic α polymorph is stable under ambient conditions.[2–4] iPP crystallizes predominately in the α form during isothermal crystallization[5] and during melt spinning of filaments.[6,7] The β polymorph is obtained upon crystallization in a temperature gradient from a sheared melt, or in the presence of β nucleating agents such as quinacridone pigment.[8–11] The γ polymorph is obtained by slow cooling of low-molecular-weight polypropylene, or by crystallization under high pressure.[12]

The mesophase, often referred to as defective phase, is formed when the melt is cooled at very high rates, usually higher than 100 °C/s,[12–15] which are commonly encountered in fiber spinning at moderate and high take-up velocities.[16] It is favored by the presence of low molecular weight distributions, and low draw-down ratios.[17,18] The mesomorphic phase has molecular ordering between that of the amorphous and of the true crystalline phase,[19,20] with molecules arranged roughly as in the α crystal, but containing defects along the chains and in the packing perpendicular to the chain direction.[21]

The crystalline content and the orientation of the iPP chain segments are known to affect the polymer mechanical properties. High crystallinity content and high orientation lead to increased strength and high modulus values. The yield stress has been put in relation with the lamellar thickness, as for example in Ref. 22 where compression molded iPP samples were studied. A dislocation-based theory similar to that developed for metallic crystals has been used to justify this dependence.[23,24] Strain hardening was not put in a definite relation with neither lamellar thickness nor percentage crystallinity.[25] Fracture and fragmentation of crystalline structures usually accompanies yielding and further plastic deformation. Phase transformations during mechanical deformation, such as the transition of β-phase to α-phase during plastic deformation at large strains results in toughening of the iPP.[26–28] The relation between microstructural evolution and mechanical behavior has been studied by many other authors, for example, Refs. 29–33. The effect of

annealing of similar spun fibers on their structure and mechanical properties has also been investigated.[34,35] The degree of crystallinity and chain orientation increase upon annealing, but the difference between the monotonic tensile properties of annealed and non-annealed fibers is small.

Nanoindentation and atomic force microscopy (AFM) have been used in the past to infer elastic-plastic properties of fibers and to allow the comparison of fiber processing outcomes.[36–41] The elastic modulus determined by AFM nanoindentation of iPP grown from the surface of carbon fibers has a value of 1.6–3 times higher in the direction perpendicular to the crystalline growth compared to that in the direction of the growth.[23] Nanoindentation was used to compare $\alpha-$ and β-type spherulites[42] and it was concluded that the β-spherulites have elastic modulus and hardness values 10 and 15% lower than the α-spherulites, respectively. Studies of the effect of cooling rate on the elastic modulus of melt solidified samples measured using AFM indentation led to the conclusion that the hardness and modulus decrease as the cooling rate increases.[43,44]

In this work, we evaluate the elastic moduli of lamellae and interlamellar regions in semicrystalline α iPP, we consider states in which the crystals are of α type and states in which the lamellae are mesomorphic, in an attempt to gain insight into the difference between the elasticity of α and meso iPP.

EXPERIMENTAL

Materials

Two commercial grades of iPP were used in this study: Pro-fax PH835, supplied by Lyondell-Basell, having molecular weight $M_w = 141{,}708$ g/mol and polydispersity index PDI = 2.33, and Exxon3854 (Achieve), supplied by Exxon-Mobil Chemical, having $M_w = 138{,}054$ g/mol and PDI = 2.05. PH835 was synthesized using the Ziegler–Natta catalyst method, while Exxon3854 was synthesized using the Metallocene catalyst. The two iPPs had melt flow rates of 35 g/10 min for PH835 and 25 g/10 min for Exxon3854. The melt flow rate was measured following the ASTM D1238 standard, using a load of 2.16 kg and the melt held at 230 °C; the melt was equilibrated at this temperature for 3 min before the test. The zero shear rate viscosity of the two iPPs in the melt state measured with an Ares-G2 rheometer was 597.4 and 614.9 Pa s at 200 °C for PH835 and Exxon3854, respectively. The longest relaxation time, τ_d, for PH835 was 5.05 ms at 180 °C, while for Exxon3854 it was 4.95 ms at the same temperature. This relaxation time was evaluated based on the storage and loss moduli, $G'(\omega)$ and $G''(\omega)$.

The iPP fibers were spun using a spinneret assembly comprising a melt extruder with a 288-hole die plate, each hole had a diameter of 0.5 mm, an air quench component along the spin line, and a fiber drawing component or aspirator, operated at specified pressure differentials. The melt fed into the extruder was at 210 °C and extruder speed was 50 rpm. The cooling air had room temperature. Fibers were collected immediately after extrusion. As they deposited on the collector belt at room temperature (the actual fiber temperature on the belt was measured to be 24 °C). The take up speeds were set to 1000 and 3000 m/min (as relevant for current industrial processes) in separate experiments and the mass throughput was 0.6 g/hole/min (172.8 g/min for the entire flow through the die) in all cases reported here. The fiber take-up speed was considered to be equal to the air velocity at the end of the aspirator. No additional heat treatment was applied to the fibers after spinning.

Structural Characterization

Raman Spectroscopy. Raman measurements were performed using a WITec Alpha300R confocal Raman microscope. A laser excitation wavelength of 532 nm was used with a lens of 300-mm focal length and 1800 lines/mm grating assembly. Each accumulated pulse had an integration time of 0.5 s and the total number of such pulses averaged to provide the final Raman signal was 50. Both fiber surface and fiber cross-sectional data was acquired at room temperature, on a thermo-electric cooled (−70 °C), back-illuminated CCD detector chip, having pixel size of 26 × 26 μm^2.

Small-Angle and Wide-Angle X-ray Scattering. X-ray scattering measurements were carried out using the NANOSTAR by Bruker AXS. It contains of a Turbo X-ray source (TXS) having a maximum energy of 5.4 kW at a beam focal spot size of 0.3 × 3 mm achieved using a three-pinhole collimator system. The diffracted patterns were recorded by a two-dimensional HI-STAR detector 1024 × 1024 pixels with photon counting ability. The distance to the small-angle X-ray scattering (SAXS) and wide angle X-ray scattering (WAXS) detectors was 1079 and 80 mm, respectively, and the collection time was 30 min. Filtered Cu-Kα radiation was used as the source with a wavelength of $\lambda = 1.54$ Å. The measurement was calibrated using several diffraction orders of silver behenate. The data reduction and image analysis included background correction, while radial and azimuthal integration of the diffractograms was performed using custom Matlab routines. Diffraction was performed on 20–30 aligned fibers at a time in order to increase signal yield.

Mechanical Characterization

Atomic Force Microscopy. The instrument used was MCR scanning probe microscope (SPM) from Park Scientific. The atomic force microscopy (AFM) cantilever used had a probe tip radius of 8 nm, tip cone angle of 40°, and a spring constant of 45 N/m. The tip height was adjusted to ensure near perpendicularity of penetration while indenting.

To insure that samples do not move during probing, fibers were mounted in epoxy. Further, the epoxy-fibers film was oxygen plasma etched for 15–30 min to expose some of the fibers. Etching has also the advantage of eliminating a thin surface layer of fibers, which may or may not have the same structure with the fiber interior. The temperature the sample is exposed to during etching was measured with a protected thermocouple, which was exposed to the plasma for the same amount of time. The maximum temperature reached was 100 °C. This annealing is not expected to produce any structural change in the fibers. Hedesiu *et al.*[45] used NMR, SAXS, and DSC to study the effect of annealing at different temperatures and time on the mobility and phase composition of iPP samples. They conclude that no annealing effects are observed in samples exposed to temperatures below 110 °C for 30 h. Bai *et al.*[46] indicate that annealing iPP for 12 h at temperatures below 110 °C does not lead to

changes in the primary DSC traces and mechanical properties. We have used Raman to probe the samples prepared for AFM indentation and concluded that the Raman spectra were identical, within the noise of the measurement, with those of the as-spun fibers, therefore confirming the conclusion of the cited annealing studies.

All surfaces were imaged using the same AFM tip before indentation to select a properly oriented region. The roughness of the sample surface was evaluated from the topographical AFM image. The effect of the sample roughness on the measured modulus was estimated as discussed in Evaluation of the Elastic Moduli of Constituent Phases section.

The indentation depth was varied in preliminary studies to determine the variation of the measured parameter with the depth. In all tests reported here, the modulus was evaluated from indents 100 nm deep performed with an indentation speed of 0.2 μm/s. The indentation depth was selected such as to minimize pile-up. Multiple indentations were performed at various locations of the same fiber. For each material studied multiple fibers were used and 50–100 indents were performed to collect sufficient statistics. The modulus of elasticity was evaluated from the initial slope of the unloading branch of the force-indentation depth curve, as usual.[36] All AFM tests were performed at room temperature.

RESULTS AND DISCUSSION

The goal of this investigation is to evaluate the elastic constants of constituent phases, the α crystal and mesophase lamellae and the associated amorphous interstices. To obtain these various states of iPP, melt spinning is used to put the material in the form of fibers. This allows reaching states in which the microstructure contains only mesophase and amorphous material, and states in which the material is predominantly a combination of α lamellae and amorphous polymer. As reviewed in the introduction, for take-up speeds in the vicinity of 1000 m/min, the microstructure contains mesophase and amorphous material, while for higher speeds, shish–kebab microstructures containing predominantly α crystals result.[47] In fibers spun at speeds larger than 1000 m/min stacks of crystalline lamellae separated by amorphous regions form. The chains in the crystalline lamellae are oriented in the flow direction, which coincides with the fiber axis. In this work, we take advantage of this almost serial lamellar arrangement which favors probing the crystalline lamellae approximately edge-on, which, in turn, makes possible the evaluation of the elasticity of α crystals in the direction perpendicular to the chain orientation.

As outlined in Experimental section, four types of samples are considered in this work: PH835 spun at 1000 and 3000 m/min take-up speeds (denoted as PH1000 and PH3000, respectively), and Exxon3854 spun at the same velocities (denoted as EX1000 and EX3000). Microstructural characterization is performed on all samples using a variety of techniques. Indentations are performed to measure the effective modulus, from which the constituent phase moduli are inferred using a statistical analysis. This last step is guided by finite element modeling of structures similar to those inferred from the result of the characterization studies.

Microstructural Characterization

Microstructural characterization of these materials has been performed before and is reported in the literature.[33,48] We also perform WAXS, SAXS, and Raman analyses to obtain reference data for the specific samples used for the AFM studies.

WAXS. The WAXS spectrum of iPP has been reported by many groups.[49–52] Figure 1(A,B) shows the spectra for our PH-1000 and PH-3000 samples. These patterns exhibit strong equatorial reflections and additional reflections at 45° with respect to the fiber direction. Figure 1(C,D) shows the corresponding integrated profiles, $I(2\theta)$, where θ is the scattering angle. Azimuthal integration was performed over the entire range of the azimuthal angle, $(0, 2\pi)$, such that both the equatorial and 45° reflections are visible in Figure 1(C,D). The curves are normalized with their respective maxima. Similar curves result for EX-1000 and EX-3000.

The broad peaks in Figure 1(C) are indicative of the dominant presence of the mesophase. The peaks are located at $2\theta = 14.6°$ and 20.6°. No crystalline peaks are observed, but a significant amorphous fraction is expected just based on the value of the minimum between the peaks.

The sharp peaks in 1(d) indicate a large crystalline content. The peak positions, $2\theta_{hkl}$, indicate the presence of the usual α phase and are identical for PH-3000 and EX-3000 ($2\theta_{hkl} =$ 14°, 16.7°, 18.4°, and 21.4° for the (110), (040), (130), and (111) reflections, respectively).This is in agreement with literature.[4] From these data, the lattice parameters of the α crystal result similar to those reported in the literature[53] and the density is computed to be 0.93 g/cm^3. This value is in the range of densities usually assigned to the iPP α crystal, that is, 0.915–0.949 g/cm^3.

The phase composition is determined by decomposing the diffraction intensity function $I(2\theta)$ in amorphous, mesomorphic and crystalline contributions, $I(2\theta)=I_a(2\theta)+I_c(2\theta)+I_m(2\theta)$. The crystalline part, $I_c(2\theta)$, is further decomposed in contributions corresponding to the peaks visible in the range of 2θ smaller than 25°. An asymmetric lorentzian profile[54] is considered for the amorphous part, $I_a(2\theta)$, the $I_m(2\theta)$ function for the mesomorphic contribution is taken from the literature[55] and each of the crystalline peaks is considered a Gaussian function of unknown width and amplitude. The relative amplitudes of the Gaussians corresponding to the crystalline peaks is defined by the α crystal spectrum of iPP from literature.[56] Only one width parameter (width-to-height ratio) is considered for all peaks when fitting the experimental data. The variables of the fitting procedure are the amplitudes of I_a, I_m, and of the (110) peak of I_c, as well as the width parameter of the crystal peaks.

Given the similarity of their diffraction spectra (Figure 1), the fractions obtained for the two resins are almost identical. PH1000 and EX1000 have 14% amorphous and 86% mesomorphic content, PH-3000 contains 57, 36, and 7% crystalline, mesomorphic, and amorphous phases, respectively, while EX-3000 contains 61, 33, and 6% crystalline, mesomorphic, and amorphous phases (Table I). The crystalline peaks width resulting

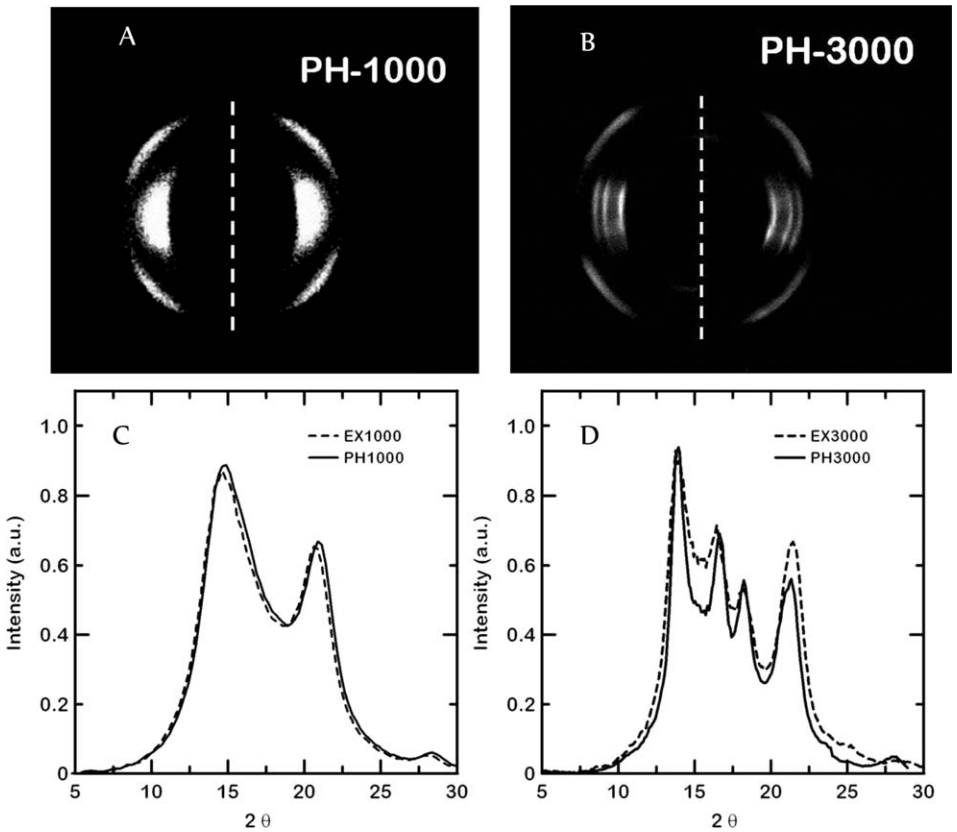

Figure 1. WAXS patterns for (A) PH-1000 and (B) PH-3000 and integrated profiles for resins spun at (C) 1000 m/min and (D) 3000 m/min. The fiber axis is indicated with dashed lines in (A) and (B).

from the fit can be used to infer the thickness of the crystalline lamellae, $\bar{L}_c$, using Scherrer's equation,[57] $\bar{L}_c = k\lambda/\beta\cos\theta$. Here, β is the peak width at half height (FWHM), in radians, after correcting for instrumental broadening, $k = 0.94$ and $\lambda = 1.54$ Å is the wavelength of the radiation. An overbar on $\bar{L}_c$ indicates the mean value of the thickness distribution function of the crystalline lamellae. The values resulting from this analysis are $\bar{L}_c$=65 and 53 Å for PH3000 and EX3000, respectively.

Raman Spectroscopy. Raman spectroscopy was also used to evaluate the crystallinity on the fiber surface and in the fiber cross section (for fibers sectioned). No significant differences were observed between the various points of the cross section, indicating the absence of any core-shell structure. The analysis of the 808–840 cm^{-1} spectral region indicated a three-phase structure consisting of a crystalline phase related to the intensity of the 808 cm^{-1} band, an isomeric defect phase related to the intensity of the 840 cm^{-1} band and an amorphous phase related to the intensity of the 830 cm^{-1} band.[35,58] Curve fitting of the frequencies in the range 800–850 cm^{-1} using a Lorentzian/Gaussian procedure yielded the actual intensities of each band, I_{808}, I_{830}, and I_{840}. These were used to compute the fractions of each phase as $\bar{X}_c = I_{808}/I_T$, $\bar{X}_a = I_{830}/I_T$, $\bar{X}_m = I_{840}/I_T$, where $I_T = I_{808} + I_{830} + I_{840}$.[58] The values for the high take-up speed are similar to those resulting from the WAXS analysis. However, while WAXS indicates a predominantly mesomorphic structure for resins processed at 1000 m/min, Raman indicates the presence of α crystals. The two characterization techniques rely on different physics to identify the quantities of interest and this leads to the discrepancy observed in Table I. These results are similar to those presented in Ref. 35.

Table I. Fractions of Crystalline, $\bar{X}_c$, and Mesomorphic, $\bar{X}_m$, Phases Obtained from the WAXS and Raman Spectroscopy Analyses

	WAXS		Raman	
iPP	$\bar{X}_c$	$\bar{X}_m$	$\bar{X}_c$	$\bar{X}_m$
PH1000	-	0.86	0.42	0.40
PH3000	0.57	0.36	0.55	0.37
EX1000	-	0.86	0.43	0.38
EX3000	0.61	0.33	0.56	0.37

SAXS Analysis and Evaluation of the Spatial Distribution of Crystallinity. SAXS was collected simultaneously with the WAXS diffractogram for all fibers. Figure 2(A,B) shows the SAXS patterns for PH-1000 and PH-3000.

These images are processed using usual methods.[59–61] The data is averaged in the azimuthal direction over a 40° angular sector centered on the equatorial line of each image (axial direction of the fiber). The wave vector-dependent scattered intensity, $I(q)$, is computed using $q = \frac{2}{\lambda}\sin\theta$, and then Lorentz corrected, $I^*(q) = q^2 I(q)$, to eliminate the large Gaussian peak at $q = 0$. The correlation function is then computed using the Weiner-

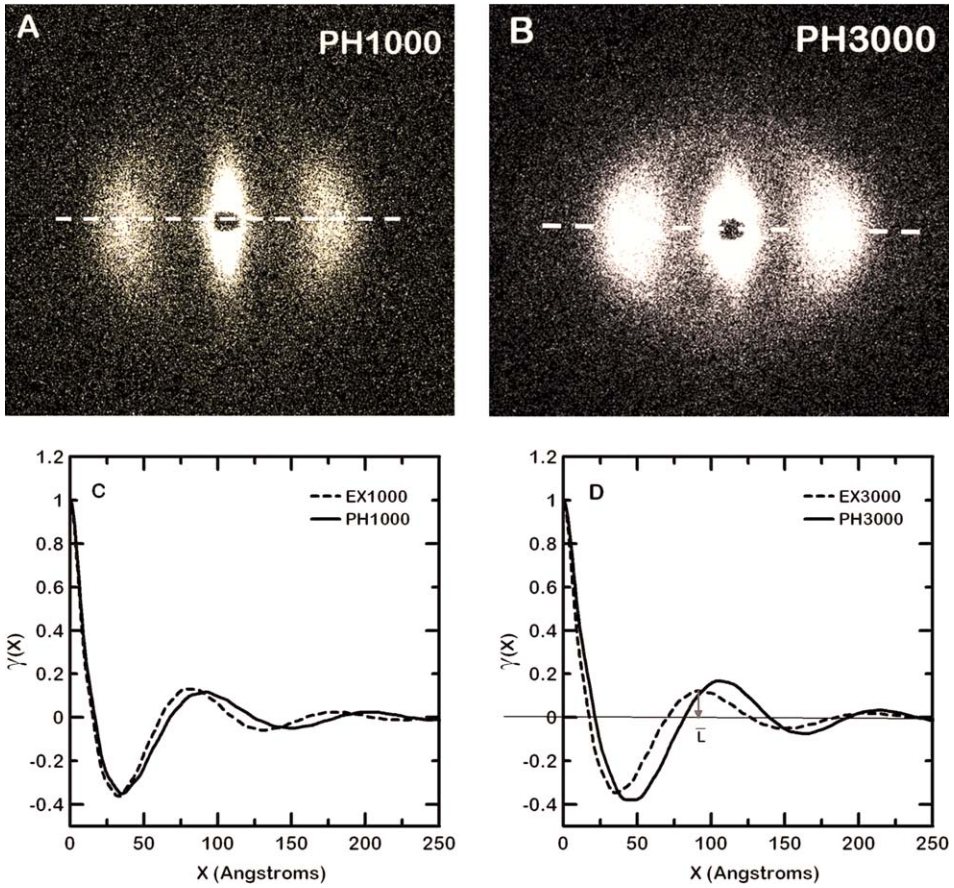

Figure 2. Unprocessed SAXS patterns for (A) PH-1000 and (B) PH-3000 and (C, D) auto-correlation functions for all types of fibers studied. The fiber axis is indicated with dashed lines in (A) and (B). The mean long period, $\bar{L}$, is shown in (D) for EX-3000. [Color figure can be viewed in the online issue, which is available at wileyonlinelibrary.com.]

Khinchin theorem as the cosine transform of $I^*(q)$, $\gamma(x)=\frac{1}{Q}\int_0^\infty I^*(q)\cos(2\pi qx)dq$, where the normalization factor, $Q=\int_0^\infty I^*(q)dq$, is known as the invariant. Since experimental data are collected only in a finite range of scattering vectors, $(q_{\min}, q_{\max})$, the experimental dataset is extended to 0 using a linear function and to infinity using a Porod function $(1/q^4)$.

Figure 2(C,D) shows the correlation function $\gamma(x)$ for the four materials studied. The usual analysis of these curves provides the long period, $\bar{L}$, which is given by the position of the first correlation peak and estimates for the thickness of the high-density and low-density lamellae, which are obtained from the correlation triangle analysis, that is, based on the slope of $\gamma(x)$ at $x=0$. The analysis provides the means of the distribution functions of these quantities. Since the analysis is not specific as to what type of material (ordered or disordered) the two thicknesses correspond to, we prefer to denote them as $\bar{L}_1$ and $\bar{L}_2$, with $\bar{L}_1+\bar{L}_2=\bar{L}$.

It is further possible to consider that the lamellae and interlamellar spacings are not of the same width in the probed domain and to inquire what are the standard deviations σ_{L_1} and σ_{L_2} characterizing these fluctuations. Hence, one accounts for the possibility that the fraction crystallinity has spatial variations associated with the fluctuations of lamellae thickness. We are interested in evaluating the standard deviation of the distribution of local fraction crystallinity values, σ_{X_c}, which is an essential parameter of the statistical analysis leading to the evaluation of lamellar elastic moduli.

To gain insight in to these issues, we use computer-generated data sets to study the effect of structural variability on $\gamma(x)$. We generate functions which take the value 1 over segments of length sampled from the probability distribution function of L_1, separated by segments of length sampled from the distribution function of L_2 over which the function takes the value zero.[59] The resulting data set is a succession of rectangular pulses of unequal width. We observe that if the standard deviations of L_1 and L_2 are different, the first minimum of $\gamma(x)$ is asymmetric. With symmetric minima, one can infer that the standard deviations are similar. In this case, the coefficient of variance, $\sigma_L/\bar{L}$, controls the decrement of $\gamma(x)$.

A further refinement can be introduced by accounting for sequences in which successive lamellae thicknesses are sampled from different distributions with different means. The resulting structure contains thick lamellae separated by thin lamellae, with the thickness of the amorphous layers between them being kept constant. This introduces an additional parameter representing the ratio of the means of these distributions, $R=\bar{L}_1'/\bar{L}_1$.

Table II. Parameters Resulting from the SAXS Analysis

				Case 1		Case 2	
iPP	$\bar{L}$ [nm]	$\omega=\frac{\sigma_L}{\bar{L}}$	R	$\bar{X}_c$ or $\bar{X}_m$	ω_{X_c} or ω_{X_m}	$\bar{X}_c$ or $\bar{X}_m$	ω_{X_c} or ω_{X_m}
PH1000	9.3	0.5	1	0.61	0.34	0.43	0.49
PH3000	10.6	0.4	0.9	0.62	0.25	0.4	0.38
EX1000	8.3	0.45	1	0.6	0.28	0.4	0.44
EX3000	9.5	0.45	0.85	0.62	0.28	0.41	0.44

As ratio R decreases, the periodicity shifts from $\bar{L}_1+\bar{L}_2$ to $\bar{L}_1+2\bar{L}_2$, which should be reached in the limit $R=0$. The first peak of $\gamma(x)$ moves to the left and decreases in amplitude, while the second peak moves to the left and gradually becomes dominant.

The effect of a gradual transition from the low density to the high-density regions has been discussed in the literature.[59] The presence of such interface layers increases the decrement of the correlation function. However, the effect of this parameter is much less pronounced than that of the parameters discussed above.

Based on these observations, a program was developed to analyze the experimental correlation functions. The code takes as input $\bar{L}=\bar{L}_1+\bar{L}_2$. The mean crystallinity $\bar{X}_c$ results from the correlation triangle analysis and may take two values, that is, it is equal either to $\frac{\bar{L}_1+\bar{L}_1'}{2\bar{L}}$ or to $\frac{\bar{L}_2}{\bar{L}}$. The program keeps as variables ratio R, the coefficient of variance $\frac{\sigma_L}{\bar{L}}$ (while assuming that $\frac{\sigma_L}{\bar{L}}=\frac{\sigma_{L_1'}}{\bar{L}_1'}=\frac{\sigma_{L_1}}{\bar{L}_1}=\frac{\sigma_{L_2}}{\bar{L}_2}$), and a parameter describing the thickness of the interface layers between crystalline lamellae and amorphous interlamellar domains. For each combination of variables, a 1D "microstructure" is generated in the form of a vector taking the value 0 in the interlamellar spacings, 1 inside a "lamella" and a linearly interpolated value (between 0 and 1) in the interfacial transition regions. For each lamella and interlamellar spacing the log-normal distribution function with the imposed coefficient of variation and mean is sampled to determine the width of the respective feature. The process is repeated until the entire sample of 10^4 lamellae is constructed. The correlation function for this computer-generated "microstructure" is evaluated and compared with the experimental $\gamma(x)$. The process is repeated for many combinations of the variables R, $\frac{\sigma_L}{\bar{L}}$ and the interface thickness. Specifically, we sample the three-dimensional space of the problem variables with a fine regular grid. The parameter set that leads to the best fit of the experimental correlation function is retained.

The result of the fits, that is, $\bar{L}$, $\frac{\sigma_L}{\bar{L}}$ and R, is shown in Table II. The following conclusions result:

samples containing predominantly mesophase, PH-1000 and EX-1000, produce well-defined SAXS spectra and contain lamellae of thickness comparable with that of the predominantly crystalline samples;the coefficient of variation of the lamellar thickness is similar in predominantly mesomorphic and predominantly crystalline samples and hence is not sensitive to the take-up speed, at least in the range of take-up speeds considered. Rather large coefficients of variation result in all cases;the long spacing, $\bar{L}$, increases with the take-up speed;the Ziegler-Natta PH835 resin has larger $\bar{L}$ than the metallocene EX3854 resin;for PH-1000 and EX-1000, ratio R is very close to 1, however, for PH-3000 and EX-3000, values of R in the range 0.8 to 0.9 are obtained.

Observations (a) and (b) indicate that the superstructure of the mesophase is similar to that of the α crystals and that differences observed in WAXS are due to defective packing as discussed in the literature.

The evaluation of the probability distribution function of the local fraction crystallinity, X_c, based on the distributions of L_a and L_c requires some attention. Let us assume that all these variables are lognormal distributed and further, for simplicity, assume that $\bar{L}_c\neq\bar{L}_a$ but their coefficients of variation are identical, $\frac{\sigma_{L_a}}{\bar{L}_a}=\frac{\sigma_{L_c}}{\bar{L}_c}=\omega$. One can then write the local crystallinity as $X_c=L_a/(L_a+L_c)$, work with its inverse, $1/X_c=1+L_c/L_a$, and evaluate the mean of this quantity as $\left(\frac{1}{X_c}\right)=1+\frac{\bar{L}_a}{\bar{L}_c}(1+\omega^2)$ and its standard deviation as $\sigma_{1/X_c}=\frac{\omega(1+\omega^2)}{\bar{X}_c}$. These results are then used to compute the mean of the distribution of local crystallinity, $\bar{X}_c$, and its coefficient of variation, ω_{X_c}, which read:

$$\bar{X}_c=\frac{1}{\left[1+\frac{\bar{L}_a}{\bar{L}_c}(1+\omega^2)\right]^3}\left[1+2\frac{\bar{L}_a}{\bar{L}_c}(1+\omega^2)+\left(\frac{\bar{L}_a}{\bar{L}_c}\right)^2(1+\omega^2)^4\right] \tag{1a}$$

$$\omega_{X_c}=\frac{\sigma_{X_c}}{\bar{X}_c}=\frac{1}{1+\frac{\bar{L}_a}{\bar{L}_c}(1+\omega^2)}\left[\frac{\bar{L}_a}{\bar{L}_c}\omega(1+\omega^2)\sqrt{2+\omega^2}\right] \tag{1b}$$

In the case without structural variability ($\omega\to 0$), these expressions reduce to the expected result

$\bar{X}_c=\frac{1}{1+\frac{\bar{L}_a}{\bar{L}_c}}$ and $\omega_{X_c}=0$. For $\omega=0.5$, similar to the values in Table II, the coefficient of variation of the fraction crystallinity, ω_{X_c}, takes the values 0.28, 0.41 and 0.53 for $\frac{\bar{L}_a}{\bar{L}_c}=0.5$, 1 and 2, respectively. $\bar{X}_c$ is within 10% from $\frac{1}{1+\frac{\bar{L}_a}{\bar{L}_c}}$ in all cases.

Expressions 1 are used to evaluate the mean crystallinity, $\bar{X}_c$, and its coefficient of variance, ω_{X_c}, for all cases studied. However, since the analysis cannot specifically assign one of the two values $\bar{L}_1$ or $\bar{L}_2$ to $\bar{L}_c$, we consider two cases, in which $\bar{L}_c$ takes either one value or the other. Therefore, two sets of $\bar{X}_c$ and ω_{X_c} are reported in Table II for each material studied. Note that based on the WAXS analysis, the values corresponding to PH-1000 and EX-1000 should be assigned to the mesophase and labeled $\bar{X}_m$ and ω_{X_m}.

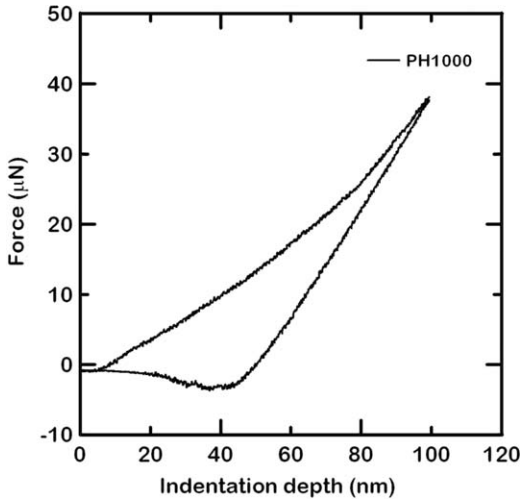

Figure 3. Typical force-indentation depth curve.

The similarity of the predicted fractions of ordered (crystalline, mesophase) and disordered (amorphous) phases is striking. All sample have either a fraction of the ordered phase of 60% with a coefficient of variation of about 0.3, or a fraction of 40% with a slightly larger coefficient of variation of approximately 0.45. This is discussed in conjunction with the data obtained from the other characterization methods in section 3.3.

The data in Table II should be also compared with those in Table I which result from the WAXS and Raman analyses. The agreement is good for the resins spun at 3000 m/min. For those spun at lower speed, WAXS indicates the predominance of the mesomorphic phase, while Raman and SAXS indicate presence of "crystals." The difference is associated with the scale at which the various techniques probe the structure.

AFM Indentation Results

Indentation using an AFM is performed to evaluate the elastic modulus. In this work we use the procedure described in Ref. 36 to interpret the indentation data. The experiment requires scanning the surface to obtain the topography before indentation, selection of the indentation point, followed by indentation and then re-scanning. The output consists of the force-indentation depth curve, $P(h)$ – a typical example is shown in Figure 3.

The effective modulus at the indentation site is computed from the upper part of the unloading branch of the force-indentation depth curve. The unloading branch is approximated with a power function, $P=\alpha(h_{\max}-h)^m$, where α and m are fitting parameters and $h_{\max}$ is the maximum value of the indentation depth. The elastic unloading stiffness is the slope of the upper portion of the unloading curve (also called the contact stiffness), $S=dP/dh$. The modulus, E, is computed from S as:

$$E=\frac{S}{2\beta}\sqrt{\frac{\pi}{A}}, \tag{2}$$

where A is the tip imprint area which is calculated by assuming a tip with vertex angle of 40°, and β is a function of the iPP Poisson ratio and the indenter tip angle. The effective modulus results after correcting the value of E by taking into account the deformation of the tip using:

$$\frac{1}{E}=\frac{1-\nu^2}{E_{\text{eff}}}+\frac{1-\nu_i^2}{E_i}. \tag{3}$$

Here, ν and ν_i are the Poisson ratios of the polymer and the AFM tip (Si), respectively, for which the values of 0.4 and 0.266 are used.[62] E_i is the modulus of Si, for which a value of 160 GPa was considered. Note that the correction based on eq. (3) is minor, given the large difference between the stiffness of the polymer and that of Si.

For each type of fiber studied, at least 100 indentations are performed. The effective modulus exhibits a broad range of values in all cases. Figure 4 shows the histograms of the measured modulus for all four materials. The mean values, $\bar{E}_{\text{eff}}$, and corresponding standard deviations, $\sigma_{E_{\text{eff}}}$, are shown in Table III.

Indentations are also performed in the cross section of the PH3000 fibers, that is, along the axis of the fiber. The histogram of the measured effective modulus, $E_{\parallel}$, is shown in Figure 5. Clear differences are observed between these data and that in Figure 4(B) which corresponds to indentations in the direction perpendicular to the fiber axis. This quantifies the degree of elastic anisotropy of the fiber. The average modulus measured in the axial direction is smaller than that measured in the transverse direction by about 52%.

When loaded in compression in the axial direction, the lamellae and the amorphous interlamellar regions are tested in series. Therefore, the smaller of the two moduli, E_a and $E_{c\parallel}$, where E_a corresponds to the amorphous region and $E_{c\parallel}$ corresponds to the crystals probed in the c-axis direction, is expected to define the result of the test. Specifically, the measured stiffness is expected to be in the interval $\left(\frac{1}{2}\min\{E_a, E_{c\parallel}\},\ \min\{E_a, E_{c\parallel}\}\right)$. The lower limit results upon assuming that $E_a=E_{c\parallel}$, while the upper limit corresponds to the assumption $E_a \ll E_{c\parallel}$. Considering that $\min\{E_a, E_{c\parallel}\}$ is equal to the stiffness of the amorphous region, E_a, and taking $E_{\parallel}$ to be equal to the mean of the distribution shown in Figure 5, E_a results in the range 1.5–3 GPa. This value is discussed further in Evaluation of the Elastic Moduli of Constituent Phases section.

The crystals are expected to be quite anisotropic. Given the preferential chain alignment in the direction of the fiber axis, the modulus measured in tension is expected to be significantly larger than the modulus measured in compression in any other direction of the crystal. A value of 15 GPa was cited in the literature for the tensile modulus of α crystals loaded along the *c*-axis.[63] The value of the modulus measured in compression is expected to be of the same order of magnitude with the stiffness in the directions perpendicular to the *c*-axis, which is what we observe.

Evaluation of the Elastic Moduli of Constituent Phases

In this section, the elastic constants of the lamellae, $E_{c\perp}$, and of the interlamellar amorphous material, E_a, are evaluated based on the AFM indentation results performed in the direction perpendicular to the *c*-axis, E_{eff} (Table III). To this end, a denoising operation is performed first.

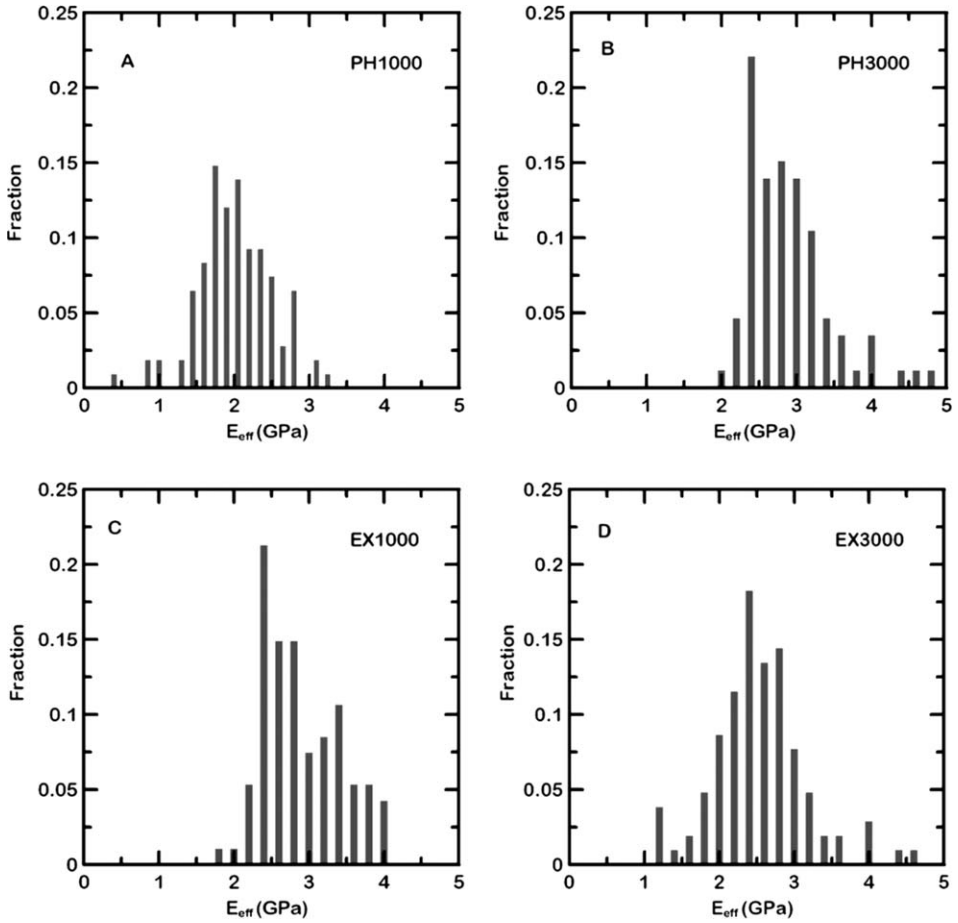

Figure 4. Histograms of the effective modulus measured by AFM indentation in the direction perpendicular to the fiber axis, for all types of fibers.

The indentation results are significantly affected by the surface roughness. This problem becomes critical when using an instrument with low column stiffness. The relatively high bending compliance of the AFM cantilever implies also relatively low torsional stiffness. Therefore, the tip-cantilever assembly could easily tilt relative to the plane defined by the cantilever axis and the indentation direction. The rougher the surface, the more pronounced the tilt is and the larger the noise expected. To eliminate the effect of the surface roughness on the data, we perform separate indentations in an epoxy surface with similar roughness as that of the fibers. The roughness was estimated directly from AFM scans. This substrate has no subsurface features, which could introduce variability. The resulting distribution function for the epoxy stiffness is significantly narrower

Table III. Mean and Standard Deviation of the Measured Effective Modulus, $\bar{E}_{\mathrm{eff}}$, $\sigma_{E_{\mathrm{eff}}}$ along with the Corrected Standard Deviation [eq. (4)] and the inferred Values of the Moduli of the Lamellae Measured in the Direction Perpendicular to the Fiber Axis, $E_{c\perp}$, and interlamellar Regions, E_a

				Case 1		Case 2	
iPP	$\bar{E}_{eff}$	$\sigma_{E_{eff}}$	$\sigma'_{E_{eff}}$	E_a	$E_{c\perp}$	E_a	$E_{c\perp}$
PH1000	2.40	0.65	0.43	1.61	2.90	2.02	2.91
PH3000	2.85	0.64	0.42	1.80	3.49	2.40	3.52
EX1000	2.80	0.90	0.76	1.17	3.89	2.11	3.84
EX3000	2.50	0.62	0.39	1.63	3.03	2.13	3.03
	Averages			1.55	3.33	2.17	3.32

All quantities correspond to compression and are given in GPa.

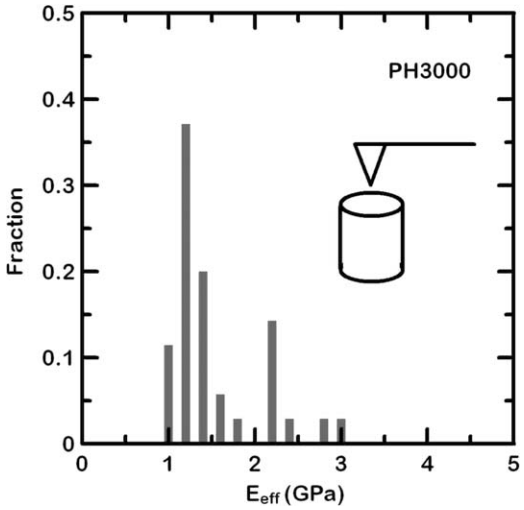

Figure 5. Histogram of the effective modulus measured by indentation in the cross-section (in the direction of the fiber axis) for PH3000 fibers.

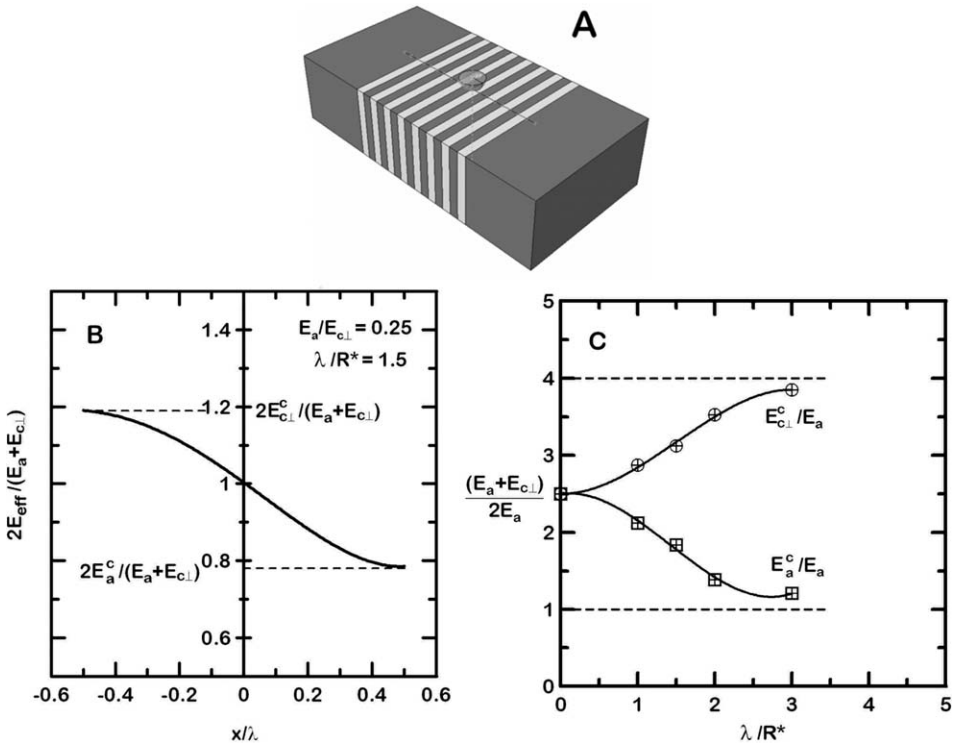

Figure 6. (A) Model used for the finite element simulation of indentation in a layered half-space with periodicity λ, (B) variation of the effective stiffness obtained from indentation with the position of the indenter axis along the x-axis, which is perpendicular to the layers [shown in (A)], and (C) variation of the limit values E^c_a and $E^c_{c\perp}$ defined in (B) with λ/R^* for the case with $\frac{E_a}{E_{c\perp}}=0.25$.

than the data presented in Figure 4. Specifically, we obtain a mean effective modulus of $\bar{E}_{\text{epoxy}}=$ 5.15 GPa with a standard deviation $\sigma_{\text{epoxy}}=$ 0.48 GPa.

Consider now that the probability distribution function of the measured quantity E_{eff} (Figure 4) which is characterized by the mean $\bar{E}_{\text{eff}}$ and the variance $\sigma^2_{E_{\text{eff}}}$, is a convolution of the actual distribution function due to the variability of the property of interest and a Gaussian noise induced by the surface roughness. These two stochastic processes are uncorrelated. To eliminate the noise due to surface roughness, it is necessary to perform the deconvolution, the result being that the distribution function representing the material property of interest is characterized by the same mean as that measured, $\bar{E}_{\text{eff}}$, and a variance which is the difference between the measured variance $\sigma^2_{E_{\text{eff}}}$ and the variance of the noise. Specifically, we obtain the corrected coefficient of variation of the distributions of E_{eff} in Figure 4, $\sigma'_{E_{\text{eff}}}$, as:

$$\frac{\sigma'_{E_{\text{eff}}}}{\bar{E}_{\text{eff}}}=\sqrt{\frac{\sigma^2_{E_{\text{eff}}}}{\bar{E}^2_{\text{eff}}}-\frac{\sigma^2_{epoxy}}{\bar{E}^2_{epoxy}}\frac{\bar{E}^2_{epoxy}}{\bar{E}^2_{eff}}}. \quad (4)$$

It is now necessary to clarify the relationship between the measured stiffness, E_{eff}, and the individual stiffness values of the lamellar, $E_{c\perp}$, and inter-lamellar, E_a, regions. It is clear that if the size of the contact, D, between the indenter and the fiber is much smaller than the thickness of the lamellae, the resulting stiffness distribution should be bimodal, with two maxima corresponding to the two types of materials. If, on the other hand, the contact is much larger than the periodicity of the microstructure, the result represents the average of the two stiffnesses, since the two types of materials are loaded in compression and are arranged in parallel relative to the loading direction.

To estimate the regime of indentation relevant for the present tests, we develop a finite element model of the microstructure. A schematic of the model is presented in Figure 6(A). A semi-infinite half-space is divided in layers of thickness λ made from linear elastic materials with alternating elastic moduli, $E_{c\perp}$ and E_a (let us assume $E_a < E_{c\perp}$) and same Poisson ratio. A spherical, rigid indenter of radius R^* is used and the indentation test is simulated by imposing traction free boundary conditions for the indented surface of the model (except in the contact region), fixed boundary conditions (imposed zero displacement) for the model surface opposite to the indented surface, and periodic boundary conditions for all lateral surfaces. We tested that the model is large enough to prevent artifacts introduced by the boundary conditions. A force P is applied on the indenter and the indentation depth, h is computed. The Hertz indentation formula[64] is then fitted to the loading branch of the force-displacement curve corresponding to the composite model. If the curve can be fitted with the Hertz formula, $P \sim h^{3/2}$, the effective stiffness results from the coefficient of proportionality in this equation.

Multiple runs are made keeping the indenter radius and indentation depth constant while varying the layer thickness λ. Since the structure is periodic, the effective modulus is also periodic with periodicity λ. Let us consider an example with $\frac{\lambda}{R^*}=1.5$ and $\frac{E_a}{E_{c\perp}}=0.25$. Figure 6(B) shows the variation of the effective

modulus function of the position of the indenter axis relative to the interface between two layers of the substrate. When the indenter axis is aligned with the center of the layer of stiffness E_a, the effective stiffness is $E_a^c > E_a$, while the value obtained when the indenter axis is aligned with the center of the other layer obeys the relation $E_{c\perp}^c < E_{c\perp}$. Indenting right above the interface leads to an effective stiffness equal to $\frac{E_a^c+E_{c\perp}^c}{2} = \frac{E_a+E_{c\perp}}{2}$.

The variation of the two limit values E_a^c and $E_{c\perp}^c$ (normalized by E_a) with the periodicity of the microstructure is shown in Figure 6(C). As discussed above, for large values of λ, the two variables converge to the stiffness of the respective layers, $E_a^c \to E_a$ and $E_{c\perp}^c \to E_{c\perp}$. When $\lambda/R^* \to 0$, that is, for very narrow layers relative to the indenter radius, the effective modulus converges to $(E_a+E_{c\perp})/2$, as expected. The curves indicate the rate of convergence to these two limits.

In our indentation experiments, the periodicity of the microstructure, λ, is on the order of 10 nm (Table II) and the contact spot size is between 50 and 100 nm. Since the contact spot size is smaller or equal to R^*, the ratio λ/R^* corresponding to the experimental conditions is smaller than 0.2. Figure 6(C) indicates that for these values of λ/R^*, the approximation that the two layers are loaded in parallel holds. For the case in which the thickness of the layers is identical, $E_{eff} \to (E_a+E_{c\perp})/2$, while for the more general case in which the layers are of different thickness and the ratio of their widths is X_c, a more general weighted average results:

$$E_{eff} = (1-X_c)E_a + X_c E_{c\perp}. \quad (5)$$

The classical weighting by volume fractions used in homogenization theory (Voigt average)[65] for various types of composites is exact in this case since the two phases are loaded in parallel.

Consider now that a large number of indents are performed and a distribution function of E_{eff} (Figure 4) results. Equation (5) indicates that the mean and variance of this distribution are given by:

$$\bar{E}_{eff} = (1-\bar{X}_c)E_a + \bar{X}_c E_{c\perp} \quad (6)$$
$$\sigma^2_{E_{eff}} = (E_{c\perp}-E_a)^2 \sigma^2_{X_c}$$

These relations allow evaluating the two quantities of interest, $E_{c\perp}$ and E_a, based on the mean and standard deviation, $\bar{E}_{eff}$ and $\sigma_{E_{eff}}$, of the distribution function of measured stiffnesses and the mean and standard deviation of the local fraction crystallinity values resulting from the SAXS experiment, $\bar{X}_c$ and σ_{X_c}.

The resulting estimates for $E_{c\perp}$ and E_a are shown in Table III. The table shows all quantities used in this evaluation, that is, $\bar{E}_{eff}$, $\sigma_{E_{eff}}$ along with the corrected standard deviation $\sigma'_{E_{eff}}$ [eq. (4)], as well as $\bar{X}_c$ and σ_{X_c} for both cases shown in Table II. Case 1 leads to mean estimates of E_a and $E_{c\perp}$ of 1.5 and 3.3 GPa, respectively. The values corresponding to Case 2 are 2.1 and 3.3 GPa, respectively. Note that the system of eq. (6) has one more solution which corresponds to $E_a > E_{c\perp}$ which is not considered and is not shown in the table.

These values should be compared with similar data reported in the literature. As reviewed in Ref. 66, the elastic modulus of the crystal in the direction perpendicular to the chains was previously estimated in a broad range: 2.9 GPa based on XRD data, 6 GPa from neutron diffraction data and between 8.5 and 18 GPa based on simulations performing 0 K energy minimization. Values between 2 and 3 GPa are suggested in Ref. 67.

The value inferred for the interlamellar regions, 1.5 and 2.1 GPa for Cases 1 and 2, are in good agreement with those inferred from the results of indentation in the fiber cross-section (1.5 to 3 GPa, section 3.2).

CONCLUSIONS

In this article, we use a statistical analysis to infer the elastic constants of the crystalline lamellae of the α crystal and of the interlamellar regions from the effective elastic moduli measured by AFM indentation. A broad range of values have been proposed in the literature for the elastic constants of crystalline lamellae. To our knowledge, no values for the elastic moduli of the interlamellar regions have been suggested (except for the fact that the interlamellar regions are expected to be amorphous and hence the elasticity of amorphous iPP should be relevant). Our measurement provides estimates for the elastic moduli obtained by direct, mechanical means. The statistical analysis developed for this purpose allows estimating properties of domains of several nm in size from measurements performed on a scale one to two orders of magnitude larger. The technique can be potentially applied to extract useful information from other data sets as well. The data also provide insight in the degree of spatial variability of the semi-crystalline structure.

ACKNOWLEDGMENTS

The authors thank Olaf Isele and Richard Hamm from Procter&Gamble for useful discussions.

REFERENCES

1. Lotz, B. *Polymer* **1998**, *39*, 4561.
2. Natta, G.; Corradini, P. *Nuovo Cimento Suppl.* **1960**, *15*, 40.
3. Wyckoff, H. W. *J. Polym. Sci.* **1962**, *62*, 83.
4. Broda, J. *J. Appl. Polym. Sci.* **2003**, *89*, 3364.
5. Kim, Y. C.; Ahn, W.; Kim, C. Y. *Polym. Eng. Sci.* **1997**, *37*, 1003.
6. Bond, E. B.; Spruiell, J. E. *J. Appl. Polym. Sci.* **2001**, *82*, 3223.
7. Nadella, H. P.; Spruiell, J. E.; White, J. L. *J. Appl. Polym. Sci.* **1978**, *22*, 3121.
8. Padden, F. J.; Keith, H. D. *J. Appl. Phys.* **1959**, *30*, 1479.
9. Varga, J.; Ehrenstein, G. W. *Polymer* **1996**, *37*, 5959.
10. Romankiewicz, A.; Sterzynski, T.; Brostow, W. *Polym. Int.* **2004**, *53*, 2086.
11. Libster, D.; Aserin, A.; Garti, N. *Polym. Adv. Tech.* **2007**, *18*, 685.
12. Mezghani, K.; Phillips, P. J. *Polymer* **1998**, *39*, 3735.
13. De Santis, F.; Adamovsky, S.; Titomanlio, G.; Schick, C. *Macromolecules* **2007**, *40*, 9026.

14. Brucato, V.; Piccarolo, S.; La Carrubba, V. *Chem. Eng. Sci.* **2002**, *57*, 4129.
15. Choi, C.; White, J. L. *Polym. Eng. Sci.* **2000**, *40*, 645.
16. Arvidson, S. A.; Khan, S. A.; Gorga, R. E. *Macromolecules* **2010**, *43*, 2916.
17. Zhang, X. Q.; Li, R. B.; Kong, L.; Wang, D. J. *Polymer* **2008**, *49*, 1350.
18. Choi, D. M.; White, J. L. *Polym. Eng. Sci.* **2004**, *44*, 210.
19. Konishi, T.; Nishida, K.; Kanaya, T.; Kaji, K. *Macromolecules* **2005**, *38*, 8749.
20. Androsch, R.; DiLorenzo, M. L.; Schick, C.; Wunderlich, B. *Polymer* **2010**, *51*, 4639.
21. Auriemma, F. D.; Rosa, C.; Corradini, P. *Adv. Polym. Sci.* **2005**, *181*, 1.
22. Sadovsky, E. A.; Cohen, S. R.; Wagner, H. D. *Appl. Phys. Lett.* **1999**, *74*, 2966.
23. Young, R. J. *Philos. Mag.* **1974**, *30*, 85.
24. Shadrake, L. G.; Guiu, F. *Philos. Mag.* **1976**, *34*, 565.
25. Schrauwen, B. A. G.; Janssen, R. P. M.; Govaert, L. E.; Meijer, H. E. H. *Macromolecules* **2004**, *37*, 6069.
26. Karger-Kocsis, J.; Varga, J. *J. Appl. Polym. Sci.* **1996**, *62*, 291.
27. Karger-Kocsis, J. *Polym. Eng. Sci.* **1996**, *36*, 203.
28. Li, J. X.; Cheung, W. L. *Polymer* **1998**, *39*, 6935.
29. Dasari, A.; Misra, R. D. K. *Mat. Sci. Eng. A* **2003**, *358*, 356.
30. Dasari, A.; Rohrmann, J.; Misra, R. D. K. *Mat. Sci. Eng. A* **2003**, *358*, 372.
31. Schrauwen, B. A. G.; van Breemen, L. C. A.; Spoelstra, A. B.; Govaert, L. E.; Peters, G. W. M.; Meijer, H. E. H. *Macromolecules* **2004**, *37*, 8618.
32. Ebert, C.; Hufenbach, W.; Langkamp, A.; Gude, M. *Polym. Test.* **2011**, *30*, 183.
33. Colombe, G.; Gree, S.; Lhost, O.; Dupire, M.; Rosenthal, M.; Ivanov, D. A. *Polymer* **2011**, *52*, 5630.
34. Osta, A. R.; Picu, C. R.; King, A.; Isele, O.; Hamm, R.; Dreher, A. *Polym. Int.* **2014**, *63*, 1816.
35. Osta, A. R.; Picu, C. R.; Isele, O.; Hamm, R. *J. Polym. Res.* **2016**, *23*, 59.
36. Oliver, W.; Pharr, G. *J. Mater. Res.* **2004**, *19*, 3.
37. Jee, A. Y.; Le, M. *Polym. Test.* **2010**, *29*, 95.
38. De Rovère, A.; Shambaugh, R. L.; O'Rear, E. A. *J. Appl. Polym. Sci.* **2000**, *77*, 1921.
39. Zhong, Q.; Innis, D.; Kjoller, K.; Elings, V. B. *Surf. Sci. Lett.* **1993**, *290*, L688.
40. Jangchud, I.; Serrano, A. M.; Eby, R. K.; Meador, M. A. *Adv. Mater. Process* **1995**, *148*, 33.
41. Miles, M. J.; Jandt, K. D.; McMaster, T. J.; Williamson, R. L. *Colloids Surf. A* **1994**, *97*, 235.
42. Labour, T.; Ferry, L.; Gauthier, C.; Hajji, P.; Vigier, G. *J. Appl. Polym. Sci.* **1999**, *74*, 195.
43. Tranchida, D.; Piccarolo, S. *Polymer* **2005**, *46*, 4032.
44. Tranchida, D.; Piccarolo, S.; Loos, J.; Alexeev, A. *Macromolecules* **2007**, *40*, 1259.
45. Hedesiu, C.; Demco, D. E.; Kleppinger, R.; Vanden Poel, G.; Gijsbers, W.; Blümich, B.; Remerie, K.; Litvinov, V. M. *Macromolecules* **2007**, *40*, 3977.
46. Bai, H.; Wang, Y.; Zhang, Z.; Han, L.; Li, Y.; Zhou, Z.; Men, Y. *Macromolecules* **2009**, *42*, 6647.
47. Choi, D.; White, J. L. *Int. Polym. Process.* **2002**, *17*, 33.
48. El-Dessouky, H. M.; Mahmoudi, M. R.; Lawrence, C. A.; Lewis, E. L.; Voice, A. M.; Ward, I. M. *Polym. Eng. Sci.* **2009**, *50*, 200.
49. Martorana, A. *Macromol. Chem. Phys.* **1997**, *198*, 597.
50. Chen, Y.; Zhong, G.; Hsiao, B. S.; Li, Z. *J. Polym. Sci. Part B: Polym. Phys.* **2013**, *51*, 1618.
51. Zhu, P. W.; Edward, G. *J. Mater. Sci.* **2008**, *43*, 6459.
52. Zhou, H.; Wilkes, G. L. *Polymer* **1997**, *38*, 5735.
53. Turner-Jones, A.; Aizlewood, J. M.; Beckett, D. R. *Makrom. Chem.* **1964**, *75*, 134.
54. Mansel, S.; Pérez, E.; Benavente, R.; Pereña, J. M.; Bello, A.; Röll, W.; Kirsten, R.; Beck, S.; Brintzinger, H. H. *Macromol. Chem. Phys.* **1999**, *200*, 1292.
55. Hedesiu, C.; Demco, D.; Kleppinger, R.; Vanden Poel, G.; Remerie, K.; Litvinov, V. M.; Blümich, B.; Steenbakkers, R. *Macromolec. Mater. Eng.* **2008**, *93*, 847.
56. Salamone, J. C. Polymeric Materials Encyclopedia; CRC Press: Boca Raton, **1996**.
57. Suryanarayana, C.; Norton, M. G. In X-ray Diffraction: A Practical Approach; Plenum Press: New York, **1998**; Part II, Module 6, pp 2017-221.
58. Nielsen, A.; Batchelder, D. N.; Pyrz, R. *Polymer* **2002**, *43*, 2671.
59. Strobl, G. R.; Schneider, M. *J. Polym. Sci. Part B: Polym. Phys.* **1980**, *18*, 1343.
60. Fischer, S.; Marti, O.; Diesner, T.; Rieger, B. *Macromolecules* **2010**, *43*, 5009.
61. Machado, G.; Kinast, E. J.; Scholten, J. D.; Thompson, A.; De Vargas, T.; Teixeira, S. R.; Samios, D. *Eur. Polym. J.* **2009**, *45*, 700.
62. Karger-Kocsis, J. In Polypropylene: An A-Z Reference; Kluwer Academic Publishers, **1999**.
63. Sawatari, C.; Matsuo, M. *Macromolecules* **1986**, *19*, 2653.
64. Hertz, H. *J. Reine Angew. Math.* **1882**, *92*, 156.
65. Dvorak, G. In Mechanics of Composite Materials; Springer: New York, **2013**.
66. Ward, I. M., Ed. Structure and Properties of Oriented Polymers, 2nd ed.; Springer Verlag: Berlin, **2012**; pp 288.
67. Harian, H. G., Ed., Handbook of Polypropylene and Polypropylene Composites, 2nd ed.; CRC Press, **2003**, p 388.